Fabrication and Photocatalytic Properties of Novel ZnO/$ZnAl_2O_4$ Nanocomposite with $ZnAl_2O_4$ Dispersed Inside ZnO Network

Xiaofei Zhao, Lei Wang, Xin Xu, Xiaodong Lei, Sailong Xu, and Fazhi Zhang
State Key Laboratory of Chemical Resource Engineering, Beijing University of Chemical Technology,
Beijing 100029, China

DOI 10.1002/aic.12597

Novel ZnO/$ZnAl_2O_4$ nanocomposites with $ZnAl_2O_4$ nanoparticles homogeneously dispersed inside a network of ZnO are fabricated by thermal treatment of a single-source precursor of ZnAl-layered double hydroxides (ZnAl-LDHs) at 800°C. The effects of the Zn/Al molar ratio of the LDH precursors on the structure, composition, morphology, textural as well as UV-absorbing properties and photocatalytic activities of the nanocomposites are investigated in detail. The results show that the ZnO/$ZnAl_2O_4$ nanocomposites derived from the ZnAl-LDHs precursors have superior photocatalytic performances to either single phase ZnO or similar ZnO/$ZnAl_2O_4$ samples fabricated by chemical coprecipitation or physical mixing method. The heterojunction nanostructure and the strong coupling between the ZnO and $ZnAl_2O_4$ phase derived from ZnAl-LDHs precursors are proposed to contribute the efficient spatial separation between the photo-generated electrons and holes, which can concomitantly improve the photocatalytic activities. © 2011 American Institute of Chemical Engineers *AIChE J,* 58: 573–582, 2012

Keywords: photocatalysis, heterojunction, layered double hydroxides, ZnO/$ZnAl_2O_4$ nanocomposites, semiconductor

Introduction

Since Fujishima and Honda reported the evolution of oxygen and hydrogen from a TiO_2 electrode under the irradiation of light in 1972,[1] the development of semiconductor photocatalysts and techniques was regarded as one effective way to solve the energy and environmental problems.[2–4] Due to the rapid recombination of photogenerated charge carriers, i.e., electrons (e^-) and holes (h^+) pairs, the photocatalytic efficiency of the single-component semiconductor was seriously impeded. To solve this problem, much efforts have been devoted to enhance the photocatalytic activity by combining of the target semiconductor with other components, such as coating of noble metal nanoparticles,[5–7] hybridizing of conjugated materials or polymers,[8–11] doping of nonmetal ions,[12–15] and coupling of other semiconductor to form nanocomposite.[16–18] Among these strategies, the synergy of the coupled semiconductor nanocomposite has been proved to be capable of alleviating the recombination of photogenerated e^- and h^+ pairs in the photocatalytic systems: after a good matching of conduction band (CB) and valence band (VB) levels, the energy gap between corresponding band levels drives the e^- and h^+ pairs from one particle to its neighbors to form a spatial separation (Figure 1). Thus, the band structure of the semiconductor itself, as well as the interaction between the two semiconductor compounds in the nanocomposite plays an important role for the photocatalytic performance.[19–22] Herein we report the fabrication of a novel ZnO/$ZnAl_2O_4$ nanocomposite with $ZnAl_2O_4$ nanoparticles homogeneously dispersed inside a network of ZnO nanoparticles

---

Correspondence concerning this article should be addressed to F. Zhang at zhangfz@mail.buct.edu.cn.

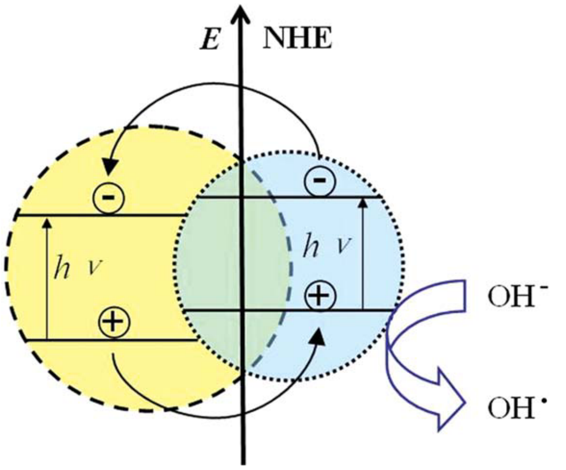

Figure 1. Schematic illumination of the coupling of two different semiconductor nanoparticle and the separation of the charge carriers, in which *E* represents the potential/eV vs. NHE.

[Color figure can be viewed in the online issue, which is available at wileyonlinelibrary.com.]

by thermal treatment of a single-source precursor of ZnAl-layered double hydroxide (ZnAl-LDH).

LDHs are a family of two-dimensional anionic clays with the general formula $[M^{2+}_{1-x}M^{3+}_{x}(OH)_2]A^{n-}_{x/n}\cdot mH_2O$, where M^{2+} and M^{3+} are di- and trivalent cations, respectively; the value of the coefficient x is equal to the molar ratio of $M^{3+}/(M^{2+}+M^{3+})$; and A^{n-} is an anion.[23] Thus, a large class of isostructural materials can be obtained by changing the metal cations, the molar ratio of M^{2+}/M^{3+}, or the interlayer anions. LDHs have a wide range of applications as catalysts or catalyst precursors,[24,25] microcontainer, and microreactor,[26,27] etc. Calcination of LDHs has been reported to be an alternative to the traditional chemical and physical methods for the fabrication of a wide variety of mixed metal oxide (MMO) nanocomposite materials composed of metal oxide and spinel phases,[28–30] and such various MMO materials displayed outstanding magnetic,[31,32] catalytic[28,33] and textual properties.[34] A recent work in our group about the thermal decomposition of ZnAl-LDH also proved that it could be a precursor material for the synthesis of ZnO-based MMO nanocomposites.[35]

Considering of ZnO nanoparticle whose band gap (E_g) is 3.2 eV exhibits comparable efficiency as TiO_2 for the photocatalytic oxidation of organic contaminations, various ZnO-based semiconductor nanocomposites have been investigated, including the mutually photosensitive components such as ZnO-TiO_2,[36] ZnO-CdS,[37] ZnO-ZnS[38] and so on. Furthermore, the coupling between ZnO and another nonsensitive semiconductor (usually have very wide band gap), e.g., In_2O_3 ($E_g = 3.6$ eV),[39] SnO_2 ($E_g = 3.8$ eV),[40] and NiO ($E_g = 3.5$ eV)[41] also has been proved to be a effective method to improve the photocatalytic activity of ZnO. Our recent observation[35] indicated that ZnO-based nanocomposite materials obtained by calcination of ZnAl-LDH precursors might be a good candidate in the photocatalysis field. In this article, a series of $ZnO/ZnAl_2O_4$ nanocomposites were fabricated by thermal treatment of ZnAl-LDH precursors with different Zn/Al molar ratio under 800°C. Subsequently, the structure, composition, morphology, textural and UV-absorbing properties of the resulting nanocomposites were systematically investigated by HRTEM, TEM, XRD, nitrogen adsorption, and UV-vis spectra techniques. Finally, the photocatalytic activities of the $ZnO/ZnAl_2O_4$ nanocomposites were evaluated by the degradation of methyl orange (MO) and the relationship between the structural features and the photocatalytic activity of the $ZnO/ZnAl_2O_4$ was discussed.

Experimental Section

Synthesis of ZnAl-LDH precursors and $ZnO/ZnAl_2O_4$ nanocomposites

The Zn_nAl-LDH precursors synthesized using the SNAS method (involving separate nucleation and aging steps) developed in our laboratory,[42] and the n value represented the Zn/Al molar ratio of as-fabricated ZnAl-LDH precursors, which were 2.0 3.0 and 4.0. A mixture of $Zn(NO_3)_2\cdot 6H_2O$ and $Al(NO_3)_3\cdot 9H_2O$ with different Zn/Al molar ratio were dissolved in deionized water to give a solution with a total cationic concentration of 1.2 M (solution *A*); and NaOH and Na_2CO_3 were dissolved in deionized water to form a mixed base solution (solution *B*). The concentrations of the base were related to those of the metal ions as follows: $[CO_3^{2-}] = 2.0\ [Al^{3+}]$, $[OH^-] = 1.6([Zn^{2+}]+[Al^{3+}])$. Solutions *A* and *B* were simultaneously added rapidly to a colloid mill with the rotor speed set at 3000 rpm and mixed for 1 min. The resulting suspension was removed and aged at 90°C for 48 h, centrifuged, washed thoroughly with distilled water and finally dried at 60°C for 24 h. The $ZnO/ZnAl_2O_4$ nanocomposites were fabricated by calcination of the as-synthesized ZnAl-LDH precursors in air at 800°C for 4 h. The resulting nanocomposites derived from LDH precursors with Zn/Al molar ratio 2.0, 3.0, and 4.0 were denoted as Zn_2Al, Zn_3Al, and Zn_4Al, respectively.

For comparison, several photocatalyst samples were prepared: (1) A single phase ZnO sample was fabricated by thermal treatment of layered zinc hydroxide nitrate, synthesized by a coprecipitation method following the procedure described in Ref. 43, at 800 °C. (2) A physical mixture sample of the single phase ZnO powder and $ZnAl_2O_4$ powder which was fabricated by the coprecipitation method described in Ref. 44 were mixed with a total Zn/Al molar ratio of 3.0 and denoted as Zn_3Al-R1. (3) A $ZnO/ZnAl_2O_4$ nanocomposite was synthesized by a coprecipitation method:[39] a mixture of $Zn(NO_3)_2\cdot 6H_2O$ and $Al(NO_3)_3\cdot 9H_2O$ with Zn/Al molar ratio of 3.0 were dissolved into deionized water to form a clear solution. Then Na_2CO_3 was added with constant stirring to the above solution until pH > 10 to ensure complete precipitation. The gel solution was aged for 24 h and then washed by deionized water for several times and then dried under 80°C; finally, the $ZnO/ZnAl_2O_4$ was obtained after annealing of such precursor under 800°C for 4 h and denoted as Zn_3Al-R2.

Characterization

Powder X-ray diffraction data (XRD) were collected on a Shimadzu XRD-6000 diffractometer under the following conditions: 40 kV, 30 mA, graphite-filtered Cu Kα radiation

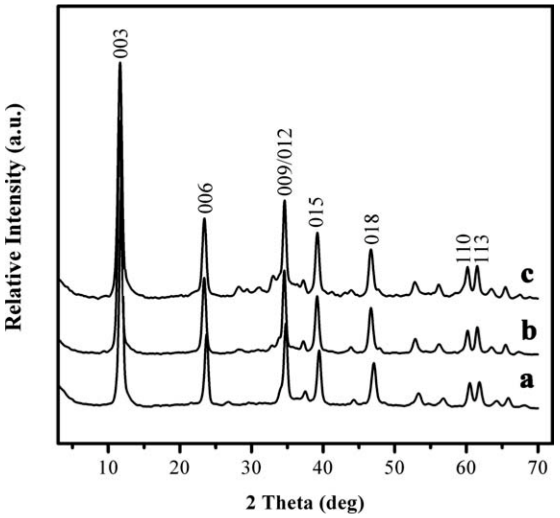

Figure 2. XRD patterns of (a) Zn_2Al-LDH, (b) Zn_3Al-LDH, and (c) Zn_4Al-LDH.

(λ = 0.15418 nm). The powder samples were step-scanned in steps of 0.04° (2θ) using a count time of 10 s/step.

Elemental analysis was performed using a Shimadzu ICPS-7500 inductively coupled plasma emission spectrometer (ICP-ES). Samples were dried at 100°C for 24 h before analysis, and solutions were prepared by dissolving the samples in dilute hydrochloric acid.

High resolution transmission electron microscopy (HRTEM) and TEM images were recorded on JEOL JEM-2010 high-resolution transmission electron microscopes. The accelerating voltage was 200 kV.

The specific surface area determination and pore volume and size analysis were performed by BET and BJH methods, with nitrogen adsorption at 77 K using a Quantachrome Autosorb-1C-VP Analyzer. Before the measurements, the samples were degassed at 200°C for 2 h.

Solid-state UV-Vis diffuse reflectance spectra were recorded at room temperature in air by means of a Shimadzu UV-2501PC spectrometer equipped with an integrating sphere attachment using $BaSO_4$ as background.

Photocatalytic reaction

The photocatalytic degradation of methylene orange (MO) on the catalyst sample was preformed under UV-light irradiation. The UV source was a 500 W high-pressure mercury lamp. Typically, a mixture of MO solution (2×10^{-5} mol/L, 100 mL) and 20 mg of catalyst was vigorously stirred in dark for 30 min until establishing an adsorption/desorption equilibrium. Then, the reaction solution was stirred under light irradiation. At given time intervals, the solution was analyzed by measuring the absorption band maximum using a Shimadzu UV-2501PC spectrophotometer. The blank reaction was carried out following the same procedure without adding catalyst.

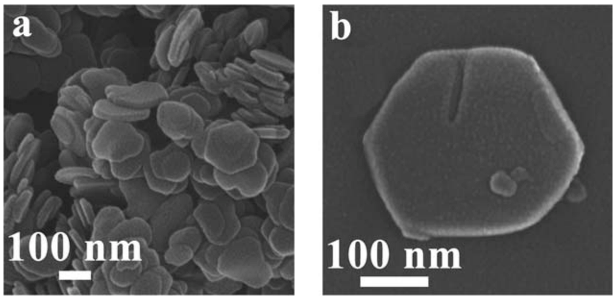

Figure 3. Typical SEM images of LDH precursor with Zn/Al molar ratio of 2.0.

Results and Discussion

Figure 2 shows XRD patterns for series of ZnAl-LDH precursors with Zn/Al molar ratio of 2.0, 3.0, and 4.0, respectively. The characteristic diffraction peaks of well-crystallized hydrotalcite-like LDH materials (JCPDS no. 38-0486) with a series of (00*l*) harmonics at low angle for the three samples are present. Assuming a 3R stacking of the layers and from the positions of the (003), (006), (009), (110) reflections, the lattice parameter *a* and *c* can be calculated.[45] The value of parameter a ($=2d_{110}$) is a function of the average radii of the metal cations while the value of parameter c ($=3d_{003} = 6d_{006} = 9d_{009}$) is a function of the average charge of the metal cations, the nature of the interlayer anion and the water content. Due to the ionic radii for Zn^{2+} (0.74 Å) is larger than that of Al^{3+} (0.50 Å), the *a* decreases from 0.302 to 0.328 nm with the Zn/Al molar ratio increasing from 2.0 to 4.0; meanwhile, the increase in lattice parameter *c* from 2.229 to 2.256 nm with increasing Zn^{2+}/Al^{3+} ratio is consistent with the decrease in Coulombic attractive force between the negative charged interlayer anions and the positively charged brucite-like layers (Table 1). Moreover, the average crystallite size in the *c* direction was calculated by means of the Scherrer equation, as shown in Table 1. The actual Zn/Al molar ratios in the obtained ZnAl-LDH precursors were estimated by elemental analysis, which is in good accordance with the Zn/Al molar ratio in initial nitrate salt

Table 1. Properties of ZnAl-LDH Precursors

Sample	Actual Zn/Al Molar Ratio in Product	Basal Spacing (nm)	Average Crystallite Size in *c* Direction*	d_{110} (nm)	Lattice Parameter (nm) $a^{\dagger}$	$C^{\ddagger}$
Zn_2Al-LDH	1.9	0.743	25.11	0.151	0.302	2.229
Zn_3Al-LDH	2.8	0.748	20.31	0.157	0.314	2.244
Zn_4Al-LDH	3.8	0.752	21.77	0.164	0.328	2.256

*Value calculated from the values of the full-width at half-maximum (fwhm) of the (003) and (006) diffraction peaks from the Scherrer equation.
†$a = 2d_{110}$.
‡c = average value calculated from (003), (006), and (009) reflections.

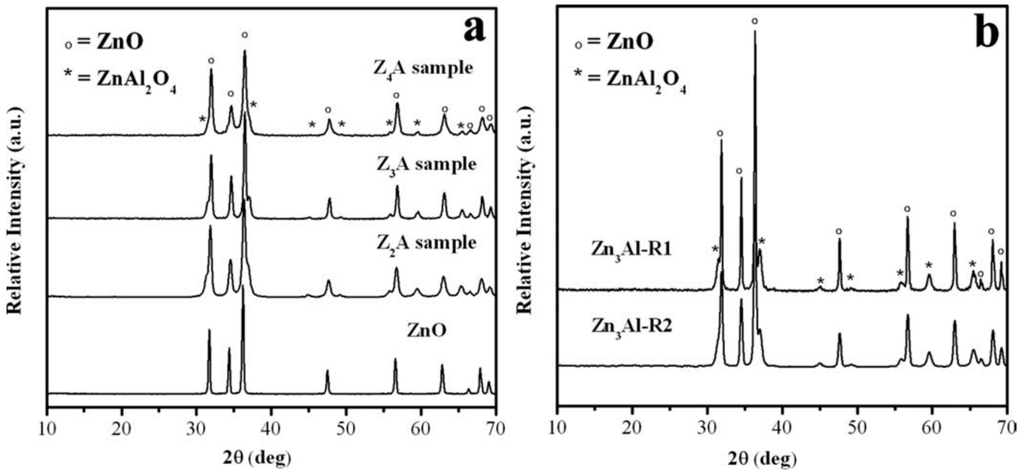

Figure 4. XRD patterns of (a) $ZnO/ZnAl_2O_4$ nanocomposites derived from LDH precursor with different Zn/Al molar ratio and ZnO sample fabricated by thermal treatment of layered zinc hydroxide nitrate at same temperature is shown for comparison and (b) for Zn_3Al-R1 and Zn_3Al-R2 samples.

solutions. The morphology of ZnAl-LDH precursors was characterized by SEM (Figure 3). The characteristic hexagonal plate-like morphology of LDH crystallite is clearly observed and the diameter of the basal plane ranges from 150 to 300 nm; the thickness of the plates is in the range of 20–30 nm, which is in good agreement with the results calculated from XRD.

Thermal treatment of the ZnAl-LDH precursors was carried out under 800°C and the XRD patterns of the resulting $ZnO/ZnAl_2O_4$ nanocomposites are shown in Figure 4a. The characteristic XRD reflection peaks for ZnO and $ZnAl_2O_4$ were observed in each case. Reducing of Zn/Al molar ratio caused an enhancement of the intensity and a sharpening of the peaks of the (220), (311), (422), (511), and (440) reflections of $ZnAl_2O_4$, indicating an increase of $ZnAl_2O_4$ amounts in the final samples. In fact, based on the decomposition equation of ZnAl-LDH (equation 1), the molar ratio of ZnO to $ZnAl_2O_4$ in the final composites from the ZnAl-LDH precursors with Zn/Al ratio of 2.0, 3.0, and 4.0 is 3.0, 5.0, and 7.0, respectively.

$$\begin{aligned}&Zn_nAl(OH)_{(2n+2)}(CO_3)_{0.5}\cdot mH_2O \longrightarrow (n-0.5)\ ZnO\\&\quad + 0.5\ ZnAl_2O_4 + 0.5\ CO_2 + (n+m+1)\ \ H_2O\\&\quad (n=2,3,\ \text{or}\ 4) \qquad (1)\end{aligned}$$

The crystalline sizes of ZnO and $ZnAl_2O_4$ in the three samples were estimated from XRD reflections by the Scherrer equation (Table 2). The particle sizes of both ZnO and $ZnAl_2O_4$ are ranged from 15 to 25 nm for the three composites. In comparison, the corresponding XRD pattern for the single phase ZnO sample derived from calcination of layered zinc hydroxide nitrate precursor at 800°C is much sharper, which indicates the larger crystallite size for the ZnO sample. As calculated by the Scherrer formula, the average crystallite size is about 51.7 nm, which is much bigger than the ZnO decomposed from the ZnAl-LDH precursors. Moreover, XRD patterns for both Zn_3Al-R1 and Zn_3Al-R2 are also shown in Figure 4b. As can be seen, diffraction peaks of ZnO and $ZnAl_2O_4$ of both samples are sharp and intense, and the bigger particle size of ZnO and $ZnAl_2O_4$ (shown in Table 2) suggests the occurring of phase sintering and separation compared with the ones calcined from ZnAl-LDH precursor with same Zn/Al molar ratio. Such results indicates that, compared with other methods (mechanical mixing or chemical coprecipitation method), the $ZnO/ZnAl_2O_4$ nanocomposite derived from series of ZnAl-LDHs precursors show higher thermal stability. According to the decoration model for the crystal growth mechanism from LDH precursors by calcination,[46] the remarkable particle-boundary mobility and the segregation and inhibition effects on the crystal growth lead to the high thermal stability and resistance to sintering of LDH under high temperature.

More detailed structural and morphology information about the $ZnO/ZnAl_2O_4$ nanocomposites was provided by (HR)TEM (Figure 5). For the Zn_3Al and Zn_4Al samples derived from LDH precursors with Zn/Al molar ratio 3.0 and 4.0, respectively, the plate-like morphology of LDH precursor is well maintained after the thermal treatment at 800°C. According to our previous work,[11] the thermal

Table 2. Textural Properties of $ZnO/ZnAl_2O_4$ Nanocomposites Derived from LDH Precursor with Different Zn/Al Molar Ratio

Sample	Particle Size of ZnO (nm)*	Particle Size of $ZnAl_2O_4$ (nm)†	Surface Area (m^2/g)‡	Pore Volume (cm^3/g)§
Zn_2Al	17.8	18.9	28.6	0.26
Zn_3Al	18.4	20.6	22.2	0.43
Zn_4Al	22.5	23.1	19.0	0.27
Zn_3Al-R1	47.5	32.7	23.44	0.08
Zn_3Al-R2	34.6	28.5	30.13	0.28

*Values determined using the Scherrer equation with (002), (110), and (103) reflections.

†Values determined using the Scherrer equation with (422), (440), and (400) reflections.

‡Surface area calculated from the N_2 adsorption isotherm according to the BET method.

§Pore size calculated from the N_2 desorption branch using the BJH model.

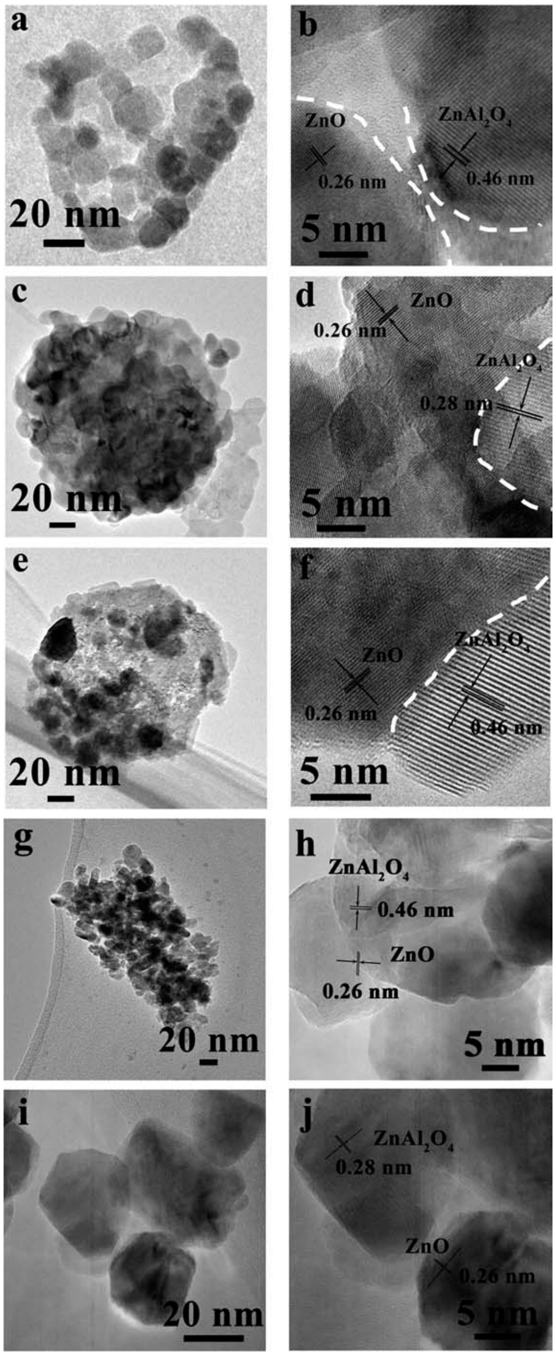

Figure 5. TEM (a, c, and e) and the HRTEM (b, d, and f) images of $ZnO/ZnAl_2O_4$ nanocomposites derived from ZnAl-LDH precursors of Zn_2Al, Zn_3Al and Zn_4Al; TEM (g, i) and the corresponding HRTEM (h, j) images of Zn_3Al-R1 and Zn_3Al-R2 samples.

decomposition of ZnAl-LDH nanoplatelets firstly led to the formation of continuous ZnO and amorphous alumina phase; with the increasing of the calcination temperature, a solid reaction between ZnO and alumina occur to form $ZnAl_2O_4$ nanoparticles which are dispersed/“planted” in the continuous ZnO phase. Thus, the growth of the $ZnAl_2O_4$ phases in the continuous network of ZnO nanoparticles can potentially have direct contact/interaction with ZnO. In addition, considering that the metal cations are uniformly distributed on a molecular level in the layers of LDH, without segregation of “lakes” of separate cations,[47] such $ZnAl_2O_4$ nanoparticles may be homogeneously dispersed inside the ZnO network. The TEM exhibit that the average particle sizes of both ZnO and $ZnAl_2O_4$ particles range from 20 to 25 nm for the two Zn_3Al and Zn_4Al samples, which are in good agreement with the results of XRD. Examination of the HRTEM images reveals that both ZnO and $ZnAl_2O_4$ phase are highly crystallized and form a heterojunction nanostructure as evidenced by well-defined lattice fringes in some regions: the spacing of 0.26 nm depicts the lattice-resolved (001) crystalline plane of ZnO phase, and the spacing value of 0.28 and 0.46 nm corresponds to the (220) and (111) facets of $ZnAl_2O_4$ phase, respectively. However, for the Zn_2Al sample, the TEM shows that although the plate-like morphology is still preserved, the platelet is loosely accumulated by ZnO and $ZnAl_2O_4$ nanoparticles. Meanwhile, HRTEM for the Zn_2Al sample shows no heterojunction structure exists between ZnO and $ZnAl_2O_4$ particles. Such results indicate that, with the increase of Al^{3+} in the ZnAl-LDH precursor, a phase segregation phenomenon occurs during the thermal treatment process, and ZnO and ZnAl2O4 nanoparticles are “separated” with each other. For comparison, TEM (Figures 5g,i) and HRTEM (Figures 5h,j) images of both Zn_3Al-R1 and Zn_3Al-R2 are also provided. As can be seen, although the lattice fringes of ZnO and $ZnAl_2O_4$ can be clearly observed, the particles are separated with each other and no heterojunction nanostructure exists in both samples.

The textural properties of the $ZnO/ZnAl_2O_4$ nanocomposites from different ZnAl-LDH precursors were investigated by the nitrogen sorption measurements, and the pore size distributions were determined by means of the BJH model from the desorption branches of the nitrogen sorption isotherms, as shown in Figure 6a and Table 2. All the $ZnO/ZnAl_2O_4$ samples have a type IV isotherm with a H_3 type hysteresis loop that does not exhibit any limiting adsorption at high P/P_0. This is commonly observed with aggregates of plate-like particles giving rise to slit-shaped pores, indicating that the plate morphology of the LDH precursors has been retained in the calcined mixture.[48,49] At the same time, the surface area of the calcined samples decreases from 28.6 to 19.0 m^2/g with the ZnO to $ZnAl_2O_4$ molar ratio in the final nanocomposites increases. We believe that such phenomena are closely related with the structural feature of different $ZnO/ZnAl_2O_4$ nanocomposites after calcination: as shown in TEM images, the higher amounts of $ZnAl_2O_4$ nanoparticles in Zn_2Al sample may result in the breaking of the continuous ZnO phase, leading to the increase of surface area. Meanwhile, all $ZnO/ZnAl_2O_4$ nanocomposites display pore diameter and broader distribution in the range of 3–100 nm. Figure 6b display the textual properties of both Zn_3Al-R1 and Zn_3Al-R2 samples: the hysteresis loops belong to H_1 type and H_3 type for Zn_3Al-R1 and Zn_3Al-R2, respectively; and the distribution of pore diameter are in the range of mesopore. Meanwhile, after the similar calcination process, the surface area of both Zn_3Al-R1 and Zn_3Al-R2 exhibits very close to that of the series of $ZnO/ZnAl_2O_4$

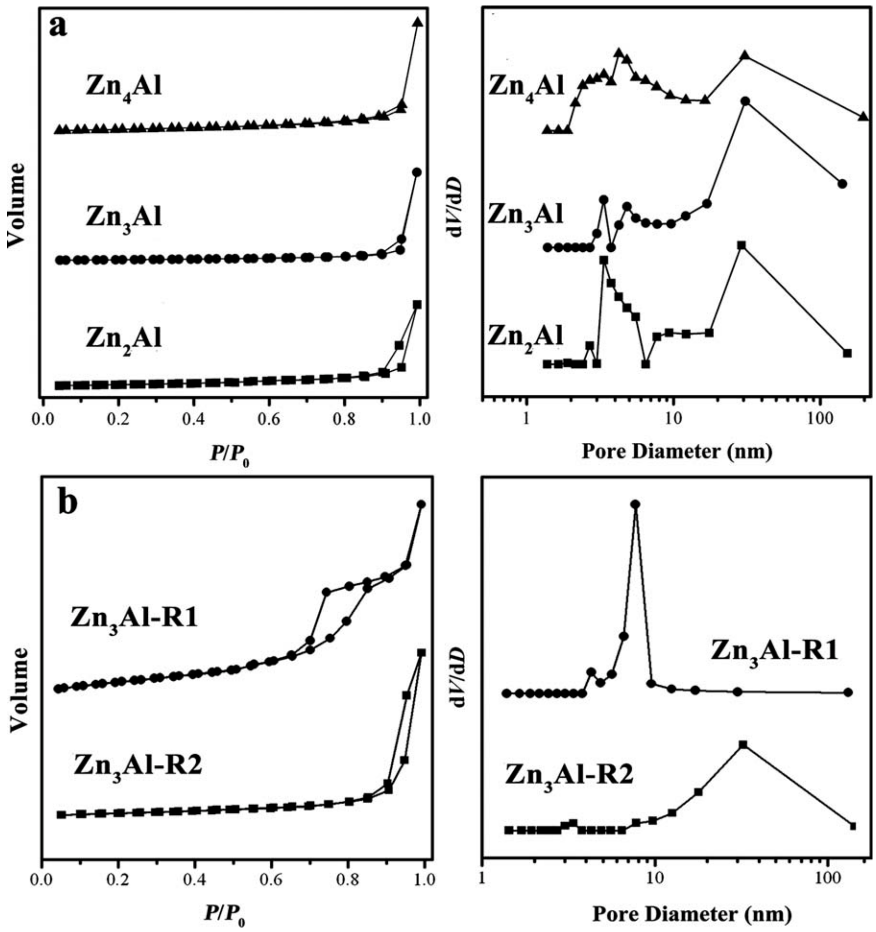

Figure 6. N_2 sorption isotherms (a left and b left) of $ZnO/ZnAl_2O_4$ nanocomposites derived from LDH precursor with different Zn/Al molar ratio and $ZnO/ZnAl_2O_4$ samples fabricated by different methods, and the corresponding pore size distributions (a right and b right).

nanocomposites derived from ZnAl-LDHs precursors, as can be seen in Table 2.

The photocatalytic activities of the $ZnO/ZnAl_2O_4$ nanocomposites were evaluated by the photodegrading organic dye of MO. Figure 7 shows the typical absorption spectra of aqueous solution of MO in the presence of the $ZnO/ZnAl_2O_4$ nanocomposites derived from Zn_3Al-LDH sample under UV irradiation at different periods of time. The major absorption peak at 464 nm corresponding to the MO molecules decreases rapidly and shifts considerably toward the blue region during the course of the photoassisted degradation. As shown in Figure 8a, the fractions of the MO dye decomposed after 1 h are estimated to be 88.5%, 76.3%, and 58.6% for the Zn_3Al, Zn_4Al, and Zn_2Al sample, respectively, all of which are higher than that of the blank experiment (3.3%) and the chemical coprecipitation ZnO sample (27.9%). The relationship between $\ln(C/C_0)$ and reaction time t (Figure 8a) shows that, the decomposition of MO with different photocatalysts accords with a pseudo first-order kinetic[50,51] and the reaction rate after the adsorption equilibrium can be express as

$$-\ln(C/C_0) = kt \tag{2}$$

Where C and C_0 are the reactant concentration at time $t = t$ and $t = 0$, respectively; k and t are the apparent reaction rate and time, respectively. A plot of $-\ln(C/C_0)$ vs. t will yield a slope of k. The apparent reaction constants (k) of MO decomposition using the photocatalysts are shown in Figure 9. Compared with pure ZnO material, all the $ZnO/ZnAl_2O_4$ nanocomposites derived from LDH precursors show higher photocatalytic activity, which is represented by larger values of k.

As a wide band-gap semiconductor (3.8 eV),[52] $ZnAl_2O_4$ mainly serves as catalysts and catalyst supports, and it also can be used as transparent conductor, dielectric or optical materials.[53] To the best of our knowledge, no systemic work has been done to investigate the photocatalytic properties of $ZnO/ZnAl_2O_4$ nanocomposites. The band energy levels and charge-transfer procedure of ZnO and $ZnAl_2O_4$ are shown in Figure 10 schematically. For ZnO, the CB bottom and the VB top lie at −4.19 and −7.39 eV, with respect to absolute vacuum scale (AVS). While for $ZnAl_2O_4$, the CB bottom and VB top lie at −3.36 and −7.16 eV vs. AVS. When ZnO and $ZnAl_2O_4$ are coupled together, photons may be absorbed in both ZnO and $ZnAl_2O_4$ and form the e^- and h^+ pairs. The electrons at the CB bottom of $ZnAl_2O_4$ would migrate to that of the ZnO; whereas holes at the VB top of $ZnAl_2O_4$

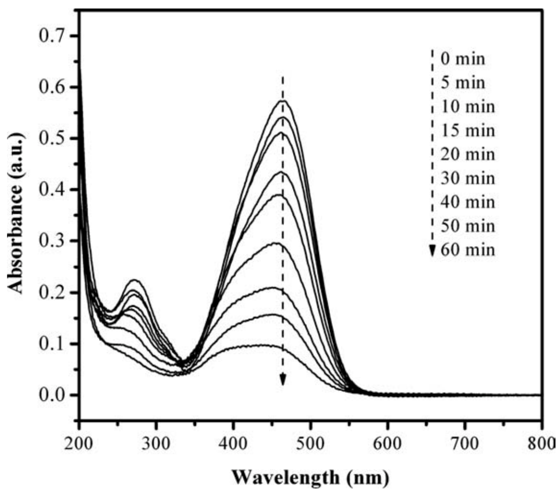

Figure 7. Absorption changes of MO solution during the photodegradation process over ZnO/$ZnAl_2O_4$ nanocomposites derived from LDH precursor with Zn/Al molar ratio of 3.0 under UV-light irradiation.

would remain there. On the other hand, the holes at the VB top of the ZnO would migrate to that of $ZnAl_2O_4$, with electrons at the CB bottom of ZnO remaining there. Such process is energetically favorable and the photogenerated e^- and h^+ pairs can be efficiently separated, which is regarded as the key factor for the enhancement of photocatalytic activities of the ZnO/$ZnAl_2O_4$ nanocomposites. All these results indicate that the coupling mode of energy gaps of ZnO and $ZnAl_2O_4$ between corresponding band levels drives the charge carriers from one particle to its neighbor to form a spatial separation between the electrons and holes.

Also, it is revealed that the effective design of a coupled semiconductor composite not only relies on the band structures of its components, but also is determined by some factors such as crystallinity, particle size and distribution, as well as loading content of the less active component.[2,54] In our system, the amount of $ZnAl_2O_4$ also shows a significant affect on the photocatalytic activity of the final ZnO/$ZnAl_2O_4$ nanocomposites: when the molar ratio of ZnO: $ZnAl_2O_4$ is 5.0, the *k* value goes through a maximum 0.037 min^{-1}, while for other samples with ZnO : $ZnAl_2O_4$ ratio of 3.0 and 7.0, the *k* value is 0.025 min^{-1} and 0.017 min^{-1}, respectively (Figure 9). All these results indicate that, compared with single phase ZnO material, the coupling effect between the interface of ZnO and $ZnAl_2O_4$ increase the lifetime of the charge carriers, which thereby transfer to adsorbed substrates and leads to the enhancement of the photocatalytic activity upon MO; such coupling effect becomes more efficient with the increase of $ZnAl_2O_4$ in the ZnO network, and therefore, the photocatalytic activity of ZnO/$ZnAl_2O_4$ nanocomposite becomes higher when the ZnO: $ZnAl_2O_4$ reaches 5.0 from 7.0. However, for the sample in which ZnO: $ZnAl_2O_4$ molar ratio of 3.0, the amount of ZnO—which is the main photocatalytic active phase, in the

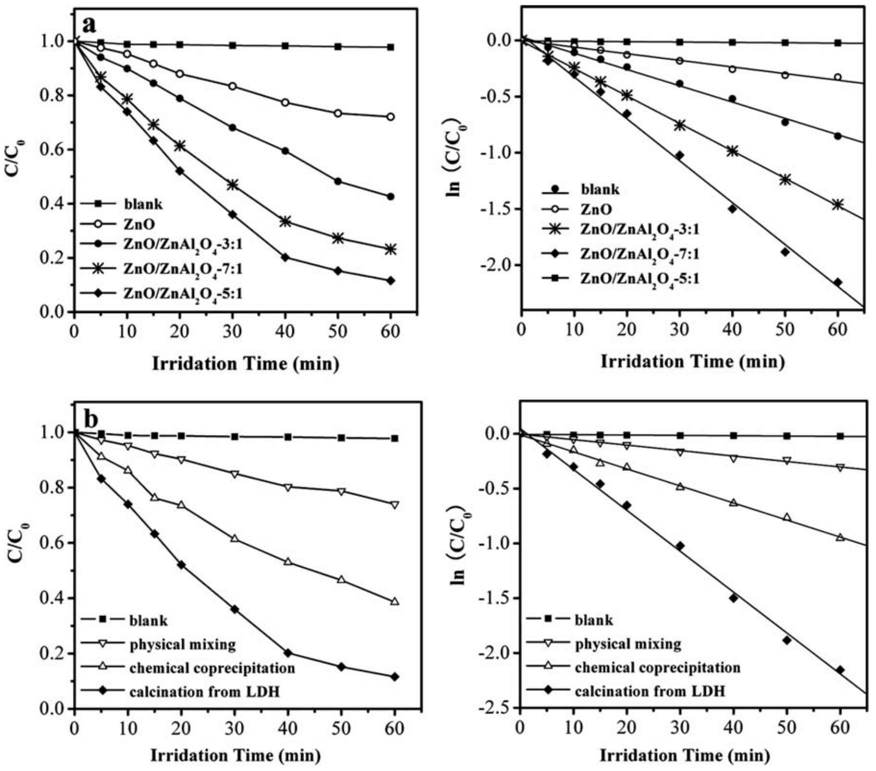

Figure 8. Photodegradation of MO monitored as the normalized concentration change vs. irradiation time with ZnO/$ZnAl_2O_4$ nanocomposites derived from LDH precursor with different Zn/Al molar ratio (a left) and ZnO/$ZnAl_2O_4$ samples fabricated by different methods (b left), and the corresponding calculated kinetic curves (a right and b right).

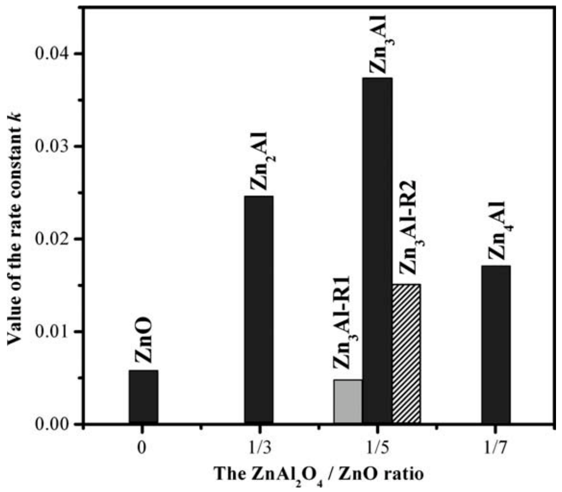

Figure 9. Comparison of rate constant (*k*) of ZnO and $ZnO/ZnAl_2O_4$ photocatalyst samples with different $ZnAl_2O_4/ZnO$ molar ratio.

final $ZnO/ZnAl_2O_4$ nanocomposite decreases, and subsequently the photocatalytic activity decreases rapidly. For comparison, the photocatalytic activities of the other two $ZnO/ZnAl_2O_4$ nanocomposites fabricated by physical mixing (Zn_3Al-R1 sample) and chemical coprecipitation (Zn_3Al-R2 sample) have been investigated. The $ZnO/ZnAl_2O_4$ nanocomposite derived from LDH precursor shows a much higher photocatalytic activity than Zn_3Al-R1 and Zn_3Al-R2 samples with the same composition (Figure 8b) and the comparison of k value are shown in Figure 9. After 1 h, the decomposition of MO only reaches 25% and 59% for the Zn_3Al-R1 and Zn_3Al-R2 samples, and the corresponding reaction constants k value of both samples are lower than that of the composite derived from Zn_3Al-LDH precursor (Figures 8b and 9). Based on the TEM results, unlike the $ZnO/ZnAl_2O_4$ nanocomposites derived from single ZnAl-LDH precursors, no heterojunction nanostructure exists for both Zn_3Al-R1 and Zn_3Al-R2 sample: ZnO and $ZnAl_2O_4$ behave as independent phase, therefore, the coupling interaction is much weaker at the interface of ZnO and $ZnAl_2O_4$ compared with the similar $ZnO/ZnAl_2O_4$ nanocompostites derived from ZnAl-LDHs precursor, and minimize the chances of charge transfer from one to the other.

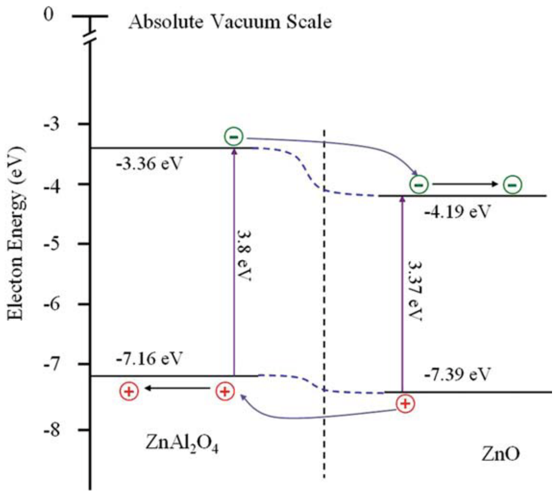

Figure 10. Schematic diagram of the band energy levels of ZnO and $ZnAl_2O_4$ semiconductors and the transfer procedure of photogenerated e^- and h^+ pairs.

[Color figure can be viewed in the online issue, which is available at wileyonlinelibrary.com.]

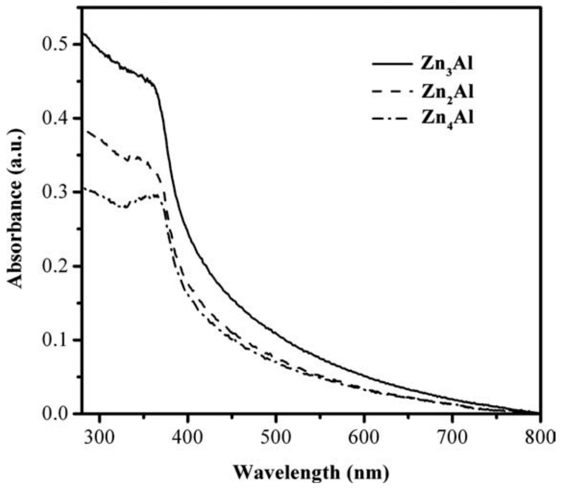

Figure 11. UV-vis spectra of different $ZnO/ZnAl_2O_4$ samples derived from the corresponding ZnAl-LDH precursors.

The relationship between the coupling effect and the $ZnO/ZnAl_2O_4$ ratio in the final nanocomposites derived from LDH precursors can be further investigated by the UV-vis spectra technology for the series of $ZnO/ZnAl_2O_4$ nanocomposites. As can be seen in Figure 11, in the visible light region (the wavelength ranging from 400 to 800 nm), no absorption in can be observed for all samples; while in the wavelength region under 400 nm, although very little changes of absorption edges of such nanocomposites can be observed as the varying amount of $ZnAl_2O_4$, the absorption intensity of the series of $ZnO/ZnAl_2O_4$ nanocomposites follows $Zn_3Al > Zn_2Al > Zn_4Al$. Such difference in the absorption of UV light under the similar conditions can be attributed to the coupling interaction between the ZnO and $ZnAl_2O_4$ phase; and the optimizing amount $ZnAl_2O_4$ in the ZnO network for Zn_3Al sample leads to the enhancement of utilization of UV light, which is subsequently conducive to the high photocatalytic activity.

Conclusions

In summary, a series of $ZnO/ZnAl_2O_4$ nanocomposites have been fabricated by thermal treatment of ZnAl-LDH precursors and the photocatalytic activity of the resultant nanocomposites has been investigated in detail. The use of single-source ZnAl-LDH precursors was of key importance in ensuring the formation of continuous ZnO network, in which the $ZnAl_2O_4$ nanoparticles were homogeneously dispersed. The direct contact/interaction of $ZnAl_2O_4$ with ZnO was expected because a heterojunction nanostructure between $ZnAl_2O_4$ and ZnO was proved by HRTEM results.

The photocatalytic results showed that the coupling of the band gap structure of both ZnO and $ZnAl_2O_4$ phase in the novel $ZnO/ZnAl_2O_4$ nanocomposite ensured the efficient separation of photogenerated e^- and h^+ pairs, which was prerequisite for the enhanced photocatalytic performance compared with single phase ZnO material. Meanwhile, by adjusting the molar ratio of Zn^{2+}/Al^{3+} to 3:1 in the ZnAl-LDH precursor, the optimized concentration of ZnO and $ZnAl_2O_4$ in the final nanocomposites led to the enhanced photocatalytic activity of such material. It was also observed that, compared with similar $ZnO/ZnAl_2O_4$ material fabricated by chemical coprecipitation or physical mixing method, a stronger coupling interaction existed at the interface in the network of ZnO with homogeneously dispersed $ZnAl_2O_4$ nanoparticles, which is consequently attributed to the enhancement of photocatalytic performance. The synthesis strategy described here might open a new route for fabrication of semiconductor nanocomposites in the development of future photocatalysts.

Acknowledgments

Financial support by the National Natural Science Foundation of China, the 973 Program (No. 2011CBA00506), the Program for New Century Excellent Talents in Universities (No. NCET-07-0055), and the Fundamental Research Funds for the Central Universities (No. ZZ0916) is gratefully acknowledged.

Literature Cited

1. Fujishima A, Honda K. Electrochemical photolysis of water at a semiconductor electrode. *Nature*. 1972;238:37–38.
2. Zhang HJ, Chen GH, Bahnemann DW. Photoelectrocatalytic materials for environmental applications. *J Mater Chem*. 2009;19:5089–5121.
3. Gogate PR, Pandit AB. Sonphotocatalytic reactors for wastewater treatment: a critical review. *AICHE J*. 2004;50:1051–1079.
4. Yang X, Ma XB, Wang SP, Gong, JL. Transesterification of dimethyl oxalate with phenol over TiO_2/SiO_2: catalyst screening and reaction optimization. *AICHE J*. 2008;54:3260–3272.
5. Chiarello GL, Aguirre MH, Selli E. Hydrogen production by photocatalytic steam reforming of methanol on noble metal-modifeied TiO_2. *J Catal*. 2010;273:182–190.
6. Ohtani B, Kakimoto M, Nishinoto S, Kagiya T. Photocatalytic reaction of neat alcohols by metal-loaded titanium(IV) oxide particles. *J Photochem Photobiol A-Chem*. 1993;70:265–272.
7. Hirakawa T, Kamat PV. Charge separation and catalytic activity of $Ag@TiO_2$ core-shell composite clusters under UV-irratiation. *J Am Chem Soc*. 2005;127:3928–3934.
8. Carneiro JT, Moulijn JA, Mul G. Photocatalytic oxidation of cyclohexane by titanim dioxide: catalyst dectivation and regeneration. *J Catal* 2010;273:99–210.
9. Zhang LW, Fu HB, Zhu YF. Efficient TiO_2 photocatalysts from surface hybridization of TiO_2 particles with graphite-like carbon. *Adv Funct Mater*. 2008;18:2180–2189.
10. Muktha B, Madras G, Guru Row TN, Scherf U, Patil S. Conjugated Polymers for photocatalysis. *J Phys Chem B*. 2007;111:7994–7998.
11. Zhang H, Zong RL, Zhu YF. Photocorrosion inhibition and photoactivity enhancement for zinc oxide via hybridization with monolayer polyaniline. *J Phys Chem C*. 2009;113:4605–4611.
12. Anpo M, Takeuchi M. The design and development of highly reactive titanium oxide photocatalysts operating under visible light irradation. *J Catal*. 2003;216:505–516.
13. Asahi R, Morikawa T, Ohwaki KA, Taga Y. Visible-light photocatalysis in nitrogen-doped titanium oxides. *Science*. 2001;293:269–271.
14. Serpone N. Is the band gap of pristine TiO_2 narrowed by anion- and cation-doping of titanium dioxide in second-generation photocatalysts? *J Phys Chem B*. 2006;110:24287–24293.
15. Ihara T, Miyoshi M, Iriyama Y, Matsumoto O, Sugihara S. Visible-light-active titanium oxide photocatalyst relized by an oxygen-deficient structure and by nitrogen doping. *Appl Catal B-Environ*. 2003;42:403–409.
16. Kisch H, Wei*β* H. Tuning photoelectrochemical and photocatalytic properties through electronic semiconductor-support interaction. *Adv Funct Mater*. 2002;12:483–488.
17. Keller V, Bernhardt P, Garin F. Photocatalytic oxidation of butyl acetate in vapor phase on TiO_2, Pt/TiO_2 and WO_3/TiO_2 catalysts. *J Catal* 2003;215:129–138.
18. Zhao W, Ma WH, Chen CC, Zhao JC, Shuai ZG. Efficient degradation of toxic organic pollutants with $Ni_2O_3/TiO_{2\text{-}x}B_x$ under visible irradiation. *J Am Chem Soc*. 2004;126:4782–4783.
19. Niu MT, Huang F, Cui LF, Huang P, Yu YL, Wang YS. Hydrothermal synthesis, structural characteristics, and enhanced photocatalysis of $SnO_2/\alpha\text{-}Fe_2O_3$ semiconductor nanoheterostructures. ACS NANO. 2010;4:681–688.
20. Liu ZY, Sun DD, Guo P, Leckie JO. An efficient bicomponent TiO_2/SnO_2 nanofiber photocatalyst fabricated by electrospinning with a side-by-side dual spinneret method. *Nano Lett*. 2007;7:1081–1085.
21. Wang DF, Zou ZG, Ye JH. Photocatalytic water spliiting with the Cr-doped $Ba_2In_2O_5/In_2O_3$ composite oxide semiconductors. *Chem Mater*. 2005;17:3255–3261.
22. Kontos AI, Likodimos V, Stegiopoulos T, Tsoukleris DS, Palaras P. Self-organized anodic TiO_2 nanotube arrays functionalized by iron oxide nanoparticles. *Chem Mater*. 2009;21:662–672.
23. Vucelic M, Jones W, Moggridge GD. Cation ordering in synthetic layered double hydroxides. *Clays Clay Miner*. 1997;45:803–813.
24. Lei XD, Zhang FZ, Yang L, Guo XX, Tian YY, Fu SS, Li F, Evans DG, Duan X. Highly crystalline activated layered double hydroxides as solid acid-base catalysts. *AIChE J*. 2007;53:932–940.
25. Hui W, Xu X, F Li. Hybird ZnAl-LDH/CNTs nanocomposites: noncovalent assembly and enhanced photodegradation performance. *AIChE J*. 2010;56:768–778.
26. Liu XL, Wei M, Li F, Duan X. Intraparticle diffusion of 1-phenyl-1, 2-ethanediol in layered double hydroxides. *AIChE J*. 2007;53:1591–1600.
27. Wei M, Zhang X, Evans DG, Duan X. Rh-TPPTS intercalated layered double hydroxides as hydroformylation catalyst. *AIChE J*. 2007;53:2916–2924.
28. Cavani F, Trifiró F, Vaccari A. Hydrotalcite anionic clays: preparation, properties and applications. *Catal Today*. 1991;11:173–301.
29. Rives V. *Layered Double Hydroxides: Present and Future*. New York: Nova Scientific Publication, 2001:1–2.
30. Evans DG, Slade, RCT. Layered double hydroxides. *Struct Bond*. 2006;119:1–234.
31. Zhao XF, Xu SL, Wang LY, Duan X, Zhang FZ. Exchange-biased $NiFe_2O_4/NiO$ nanocomposites derived from NiFe-layered double hydroxides as a single precursor. *Nano Res*. 2010;3:200–210.
32. Li F, Liu JJ, Evans, DG, Duan X. Stoichiometric synthesis of pure MFeO (M = Mg, Co, and Ni) spinel ferrites from tailored layered double hydroxide (hydrolalcite-like) precursors. *Chem Mater*. 2004;16:1597–1602.
33. Qi CX, Amphlett JC, Peppley BA. Product composition as a function of temperature over NiAl-layered double hydroxide derived catalysts in steam reforming of methanol. *Appl Catal*. 2006;302:237–243.
34. Zou L, Li F, Xiang X, Evans DG, Duan X. Self-generated template pathway to high-surface-area zinc aluminate spinel with mesopore network from a single-source inorganic precursor. *Chem Mater*. 2006;18:5852–5859.
35. Zhao XF, Zhang FZ, Xu SL, Evans DG, Duan X. From layered double hydroxides to ZnO-based mixed metal oxides by thermal decomposition: transformation mechanism and UV-blocking properties of the product. *Chem Mater*. 2010;22:3933–3942.
36. Agrawal M, Gupta S, Pich A, Zafeiropoulos NE, Stamm M. A facile approach to fabrication of $ZnO\text{-}TiO_2$ hollow spheres. *Chem Mater*. 2009;21:5343–5348.
37. Tak YJ, Kim HY, Lee DW, Yong KJ. Type-II CdS nanoparticle-ZnO nanowire heterostructure arrays fabricated by a solution process: enhanced photocatalytic activity. *Chem Commun*. 2008;8:4585–4587.
38. Jang JS, Yu CJ, Choi SH, Ji SM, Kim ES, Lee JS. Topotactic synthesis of mesoporous ZnS and ZnO nanoplates and their photocatalytic activity. *J Catal*. 2008;254:144–155.

39. Wang ZY, Huang BB, Dai Y, Qin XY, Zhang XY, Liu HX, Yu JX. Highly photocatalytic ZnO/In_2O_3 heteronanostructures synthesized by a copercipitation method. *J Phys Chem C*. 2009;113:4612–4617.
40. Zheng LR, Zheng YH, Chen CQ, Zhan YY, Lin XY, Zheng Q, Wei KM, Zhu JF. Network structured SnO_2/ZnO heterojunction nanocatalyst with high photocatalytic activity. *Inorg Chem*. 2009;48:1819–1825.
41. Hameed A, Montini T, Gombac V, Fornasiero P. Photocatalytic decolourization of dyes on NiO-ZnO nanocomposites. *Photochem Photobiol Sci*. 2009;8:677–682.
42. Zhao Y, Li F, Zhang R, Evans DG, Duan X. Preparation of layered double-hydroxide nanomaterials with a uniform crystallite size using a new method involving separate nucleation and aging steps. *Chem Mater*. 2002;14:4286–4291.
43. Newman SP, Jones W. Comparative study of some layered hydroxide salts containing exchangeable interlayer anions. *J Solid State Chem*. 1999;148:26–40.
44. van der Laag NJ, Snel MD, Magusin PCMM, De With G. Strutural, elastic, thermophysical and dielectric properties of zinc aluminate ($ZnAl_2O_4$). *J Eur Ceram Soc*. 2004;24:2417–2424.
45. Millange F, Walton RI, O'Hare D. Time-resolved in situ X-ray diffraction study of hte liquid phase reconstruction of Mg-Al-carbonate hydrotalcite-like compounds. *J Mater Chem*. 2000;10:1713–1720.
46. Rebours B, d'Espinose de la Caillerie JB, Clause O. Decoration of nickel and magnesium oxide crystallites with spinel-type phases. *J Am Chem Soc*. 1994;116:1707–1717.
47. Sideris PJ, Nielsen UG, Gan ZH, Grey CP. Mg/Al ordering in layered double hydroxides revealed by multinuclear NMR spectroscopy. *Science* 2008;321:113–117.
48. Sing KSW, Everett DH, Haul RAW, Moscou L, Pierotyi RA, Rouquérol J, Siemieniewska T. Reporting physisorption data for gas/solid systems with special reference to the determination of surface area and porosity. *Pure Appl Chem*. 1985;57:603–619.
49. Reichle WT, Kang SY, Everhardt DS. The nature of the thermal decomposition of a catalytically active anionic clay mineral. *J Catal*. 1986;101:352–359.
50. Li YJ, Li XD, Li JW, Yin J. Photocatalytic degradation of methyl orange by TiO_2-coated activated carbon and kinetic. *Water Res*. 2006;40:1119–1126.
51. Matos J, Laine J, Hermann JM. Synergy effect in the photocatalytic degradation of phenol on a suspended mixture of titania and activated carbon. *Appl Catal B: Environ*. 1998;18:281–291.
52. Sampath SK, Cordaro JF. Optical properties of zinc aluminate, zinc gallate, and zinc aluminogallate spinels. *J Am Ceram Soc*. 1998;81:649–654.
53. Wang Y, Wu K. As a whole: crystalline zinc aluminate naotube array-nanonet. *J Am Chem Soc*. 2005;127:9686–9687.
54. Zhang J, Xu Q, Feng ZC, Li MJ, Li C. Importance of the relationship between surface phases and photocatalytic activity of TiO_2. *Angew Chem Int Ed*. 2008;47:1766–1769.

Manuscript received Sep. 5, 2010, revision received Dec. 28, 2010, and final revision received Feb. 15, 2011.